Physical Science International Journal
12(2): 1-16, 2016, Article no.PSIJ.29210
ISSN: 2348-0130

SCIENCEDOMAIN *international*
www.sciencedomain.org

Ion Distribution Functions and Transport Properties in Collision-free Auroral Ionosphere Under Arbitrary Electric Fields

J. Z. G. Ma[1*] **and J. P. St.- Maurice**[2]

[1] *California Institute of Integral Studies, San Francisco, CA, 94103, USA.*
[2] *Department of Physics and Engineering Physics, University of Saskatchewan, Saskatchewan, Canada.*

Authors' contributions

This work was carried out in collaboration between the two authors. Author JZGM designed the study, performed the literature searching, theoretical modelling and numerical calculations. Author JPSM supervised all the theoretical work and simulations. Both authors read and approved the final manuscript.

Article Information

DOI: 10.9734/PSIJ/2016/29210
Editor(s):
(1) Junjie Chen, Department of Electrical Engineering, University of Texas at Arlington, USA.
(2) Abbas Mohammed, Blekinge Institute of Technology, Sweden.
Reviewers:
(1) Radosaw Jedynak, Pulaski University of Technology and Humanities, Malczewskiego, Poland.
(2) Shu-Lung Kuo, Open University of Kaohsiung, Taiwan.
Complete Peer review History: http://www.sciencedomain.org/review-history/16539

Original Research Article

Received: 29th August 2016
Accepted: 29th September 2016
Published: 13th October 2016

ABSTRACT

Filamentary space-charge aurorae bring about cylindrical structures symmetric to local geomagnetic field lines in auroral ionosphere. It produces arbitrary structured electric fields. Developed from previous work on a backward mapping technique to solve ion velocities and transport properties under both collision-free and collisional conditions in cylindrically symmetric, uniformly charged auroral ionosphere, this paper studies the collision-free case by numerically solving the Boltzmann-Vlasov equation in the presence of three arbitrarily chosen electric field configurations: (1) an electric field which is proportional to the radius inside a space charge cylinder but drops off slowly outside the cylinder; (2) an electric field which is still proportional to the radius inside the space charge cylinder but drops off more quickly out side the cylinder; and, (3) an electric

**Corresponding author: E-mail: zma@mymail.ciis.edu;*

field which is localized at the edge of the cylinder. Various shapes of non-Maxwellian ion velocity distributions and associated transport properties are obtained. In regimes where the electric field dropped outside the space-charge region, the evolving velocity distribution with time is found to have many possible types of shapes, such as, deformed pancake, horseshoe, teardrop, core-halo, etc. If the electric field drops sharply on both sides of the boundary of the region, the distribution develops into an ear-collar appearance with time. Under all electric field structures, the non-Maxwellian distributions and related transport parameters are localized to the region where the electric field permeates. The results are expected to be applicable to account for ongoing and future high-resolution observations.

Keywords: Plasma kinetic equations; space plasma physics; auroral ionosphere; F region.

2010 Physics and Astronomy Classification Scheme (PACS): 52.25.Dg, 94.05.-a, 94.20.Ac, 94.20.dj.

1 INTRODUCTION

In the local thermal equilibrium, the ion distribution function is described by a Maxwellian distribution. However, in the solar-terrestrial system, numerous non-Maxwellian distributions have been found with non-equilibrium characteristics such as beams, temperature or pitch-angle anisotropies [1-4]. In addition, in both the upstream and downstream regions of the Earth's bow shock, satellites detected that the upstream ion population has a ring-like (or, halo) distribution, while in the downstream, the distribution has a hot bell-like core and a flat tail [5,6]. Moreover, at altitudes ranging from 1000 km up through one Earth radius and beyond, there is another kind of non-Maxwellian distribution, ion conics [7]. Rocket and satellite measurements showed that ions are concentrated into cones in velocity space under different conditions, and the distribution peaks at specific pitch angles, respectively. Even below 1000 km, many direct observations have also shown the ion velocity distributions to depart from the Maxwellian shape over wide areas [8,9]. The distributions were observed whenever the ion drift exceeded the neutral thermal speed. Another crescent-shaped type of low-altitude non-Maxwellian ion velocity distribution has been found in high-resolution GEODESIC rocket experiments [10-12]. Artificial plasma disturbances can also produce non-Maxwellian distributions [13]. A possible mechanism was proposed for the deviation of the distribution from the Maxwellian equilibrium configuration [14-18]: It can occur when a minor constituent of a gas mixture experiences a force (say, $\mathbf{E} \times \mathbf{B}$ drift, where $\mathbf{E}$ and $\mathbf{B}$ represent electric and magnetic fields, respectively) that differs from the forces acting on the major constituent.

The auroral ionosphere is permeated by strong $\mathbf{E}$ the strength of which can be as high as several hundred mV/m. Contrary to those at other latitudes, these electric fields are not produced by neutral wind dynamos, but rather by processes that go back to the solar-wind–magnetosphere–ionosphere (SMI) electrodynamic coupling processes. The electrodynamics in the SMI system is described in great details [19-23]. The induced large-scale convection electric field in the high-latitude regions provides a fair context for the average flow. A multitude of measurements from low-altitude satellites, rockets, radars, and from optical means have shown that electric field measurements with insufficient temporal resolution can sometimes hide very large fluctuations and sharp transitions over a wide range of spatial and temporal scales, featured by cylindrical charge/electric field arrangements in the auroral ionosphere [24-31]. Once a localized $\mathbf{E}$ is established crossed to the ambient magnetic field $\mathbf{B}$, an $\mathbf{E} \times \mathbf{B}$ drift occur inevitably for charged particles. For strong electric fields, the drift speed can reach several km/s. This drift is considerable compared to the normal ion thermal speed and compared to the thermal speed of the neutral gas with which the ions collide. As a result, there can be strong deviations for ions from a thermal (Maxwellian) velocity distributions under both the collisional and collision-free conditions, the later of which applies to time scales shorter than a collision time, while electrons are not influenced due to

their much higher thermal speeds of tens of km/s [32]. Previous studies focused on a uniform electric field in both collisional and collision-free cases [16,33-40].

The observed cylindrical geometries have different scales. Of large scale structures are convection vortices (1000-3000 km in size), as reported and studied by a number of authors [29,41]; smaller cylindrical regions are also known to exist, for example in auroral rays [42]. The smallest structures that we are aware of can be as small as 10 to 20 m, and have been described as lower hybrid cavities [43]. We thus turn our attention to the ion velocity distributions and related transport properties that one should expect in the auroral plasma in a cylindrical frame, rather than a Cartesian one. From a review of similar problems studied in other types of plasmas, e.g., fusion plasma [44-48], we realize that the complexity of the calculation in a cylindrical geometry requires that we approach the cylindrical geometry through a series of incremental steps, so as to be able to understand the physics and develop suitable approaches, and, based on which to solve more realistic problems.

The first step was already done [49] (hereafter referred as Paper 1) to dealt with the most basic problem we were able to solve towards the goal to gain important insights into the more complicated situations, while still obtaining complete analytical solutions: We tackled a situation for which the strength of the ambient electric field is proportional to the radius of the cylinder, but is constant in time. We focused on ions that are well inside the cylinder, thereby neglecting radial edge effects and features associated with the decaying field outside the cylinder. We assumed that the cylinder has negative space charges due to electron precipitation, and these electrons need not exceed the ambient density by more than one charge in 10^5. We solved a collision-free problem, with an underlying physical model that a time scale considered is much shorter than the ion gyroperiod. The ambient electrons, with their small gyroradii and large thermal speeds, can be assumed to simply remain Maxwellian while experiencing $\mathbf{E} \times \mathbf{B}$ drift in response to the radially linear $\mathbf{E}$ produced by the uniform space charges. In that initial work, $\mathbf{E}$-field is assumed to be maintained, irrespective of the ion response. The solutions thus obtained have proved useful for more realistic applications such as in a collisional case [50].

Owing to the fact that (1) understanding velocity distributions is very important if we are to understand the small-scale physics and the fundamental measurements made by incoherent scatter radars, rockets, and satellites; (2) in physics, knowing what creates the distribution will tell us about the forces that act at any given instant; and (3) in experiments, we should rely on a known velocity distribution with the knowledge that we have a good command of what we measure, e.g., the temperature, compositions, etc., the purpose of this paper is to expand the knowledge beyond our earlier work [49,50] to answer the following question: in the presence of large electric fields (in the order of 50 mV/m) in the collision-free ionospheric F with arbitrary shears in the cylindrical geometry (applicable to altitudes higher than 140 km), how the non-Maxwellian ion velocity distributions and bulk properties evolve under arbitrarily excited ionospheric electric field profiles. The ultimate goal of this study is to set up a data-fit modelling to the ongoing and future high-resolution observations (like FAST, Cluster) of various electric field structures, therefore, to elucidate what an interplay is between the auroral ionospheric plasma and the $\mathbf{E} \times \mathbf{B}$ drift which affects the ion velocity distribution and transport properties in the presence of the observed arbitrary transverse electric fields that change radially in regimes where the electric field changes in different shapes in space. Compared with the previous work, the new consideration is now more complicated because the space-charge cylinder no longer has an infinite radius as before. This forces the electric field strength to change arbitrarily in space, and the ion orbits are no longer locked in phase, except, maybe, in the extreme inner part of the cylinder. Elsewhere, ions that start at different radial distances will feel different oscillation frequencies. The layout of the paper is as follows. Section 2 generalizes Paper 1's analytical work by introducing a semi-numerical "backward ray-tracking" approach. Section 3 gives the algebra to calculate various shapes of ion velocity distribution functions, as well as

Table 1. List of variables with physical explanations

B	auroral geomagnetic field	B	magnitude of **B**
c_k	dimensionless coefficient related to K	**E**	auroral electric field
e	elementary charge	E_c	characteristic electric field at R_c
E_r	radial magnitude of **E**	$f(r)$	electric field function, E_r/E_c
$\hat{\mathbf{r}}$	radial unit vector	f_0	O^+ initial distribution function
f_i	O^+ distribution function	$\mathbf{r}, \mathbf{v}$	phase-space position and velocity vectors
$\mathbf{r}_0, \mathbf{v}_0$	initial $\mathbf{r}, \mathbf{v}$	K	angular momentum
m_i	O^+ mass	n_i	O^+ density
n_0	initial density	P	potential energy
P_r	potential energy at r	P_{r0}	potential energy at r_0
$p_{rr}, p_{\phi\phi}$	components of pressure tensor	P_{rr0}	potential energy difference from r_0 to r
q_r, q_ϕ	components of heat flux	r, ϕ, z	cylindrical coordinates
r_0	initial radial position	R_c	cylindrical radius at which $E_r = -E_c$
T_r, T_ϕ	T_i components	$v_{\mathrm{d}r}, v_{\mathrm{d}\phi}$	drift velocity components
v_r, v_ϕ	components of $\mathbf{v}_i$	$v_{r0}, v_{\phi 0}$	initial v_r, v_ϕ
φ	scalar potential	ω, Ω_i	O^+ cyclotron and gyro-frequency

transport properties at the same time. Section 4 presents simulation results under different electric field models which vary nonlinearly with radius. Section 5 summarizes the work and discusses some important extensions based on what we obtained. Section 6 presents conclusions. Throughout the paper, SI units are used. Table 1 gives a list of variables used in the paper, along with their physical explanations.

2 GENERALIZED ELECTRIC FIELD MODEL AND EQUATIONS OF MOTION

For an arbitrary electric field structure, the cylindrically symmetric space charges are no longer extending to infinity but localized to form a cylinder in real space. Various situations are possible for the electric field strength as a function of radial distance. These can, for instance, be a negative charge density peaking near the edge of the cylinder, or, fast or slow changing profile crossing the edge, etc. Different charge density distributions produce different space-charge electric fields. The general problem is simply described by

$$\mathbf{E} = E_r \hat{\mathbf{r}} = E_c \cdot f(r)\, \hat{\mathbf{r}} \tag{2.1}$$

in which E_r denotes a radial electric field strength with a characteristic value E_c at a characteristic radius R_c, $f(r)$ is constant in time, but an arbitrary radial function versus r/R_c, defined as $f(r) = E_r/E_c$. Fig. 1 gives several examples of arbitrary $f(r)$ profiles that will be considered in this paper. For comparison, the linear electric field used in [49,50] is also given in the figure.

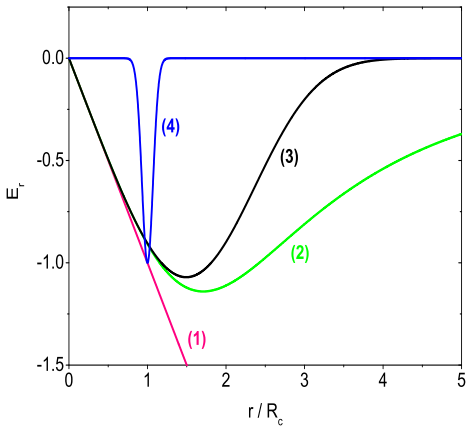

Fig. 1. Arbitrary radial electric field examples which are constant in time:

(1) $E_r = -E_c(r/R_c)$**;**
(2) $E_r = -E_c(r/R_c)/[1 + 0.1\,(r/R_c)^3]$**;**
(3) $E_r = -E_c(r/R_c)e^{-0.1(r/R_c)^3}$**; and,**
(4) $E_r = -E_c e^{-(r/R_c-1)^2/0.1^2}$**.**

As discussed in Paper 1, the ion velocity distribution is evidentally affected by the electrostatic potential energy P. The change in P as an ion moves from r_0 to r is given by

$$\left.\begin{array}{l} P_{rr_0} = P_r - P_{r_0} = e[\varphi(r) - \varphi(r_0)] = \\ = e\int_{r_0}^{r} E_r \mathrm{d}r = eE_c \int_{r_0}^{r} f(r)\mathrm{d}r \end{array}\right\} \tag{2.2}$$

For an electric field proportional to radius as supposed in Paper 1, $f(r) = r/R_c$, we have obtained

$$\left.\begin{array}{l} P_{rr_0} = \frac{1}{2} eE_c R_c \left[\left(\frac{r}{R_c}\right)^2 - \left(\frac{r_0}{R_c}\right)^2\right] = \\ = \frac{1}{2} m_i \frac{E_c}{B} R_c \Omega_i \left[\left(\frac{r}{R_c}\right)^2 - \left(\frac{r_0}{R_c}\right)^2\right] \end{array}\right\} \tag{2.3}$$

For electric fields unproportional to radius, however, the potential energy may not take such a simple analytical shape. Furthermore, even even for simple cases [e.g., $E_r = E_c(R_c/r)$], we still do not know how to connect r to r_0 and then to determine the potential energy. The problem gets worse for the "exponential" or the "cube" electric field structures introduced in Fig.2. However, this relation can be provided by solving the equation of motion analytically or numerically.

The equation of motion in an arbitrary radial electric field has the form [e.g., Eq.(2.5) in Paper 1]

$$\left.\begin{array}{l} \frac{\mathrm{d}r}{\mathrm{d}t} = v_r \\ \frac{\mathrm{d}v_r}{\mathrm{d}t} = -\left(\frac{\Omega_i}{2}\right)^2 r - \frac{E_c}{B}\Omega_i \cdot f(r) + \frac{K^2}{m_i^2 r^3} \\ \frac{\mathrm{d}\phi}{\mathrm{d}t} = \omega = \frac{K}{m_i r^2} - \frac{1}{2}\Omega_i \end{array}\right\} \tag{2.4}$$

In this set of differential equations of motion, the exact relation between the effective gyro-frequency ω and the magnetic gyro-frequency Ω_i is unknown. We therefore choose Ω_i as the timescale parameter in the numerical calculations. Using the "backward ray-tracing" technique, Eq.(2.4) becomes

$$\left.\begin{array}{l} \frac{\mathrm{d}r_0}{\mathrm{d}t} = -\frac{2\pi}{R_c\Omega_i} v_{r0} \\ \frac{\mathrm{d}v_{r0}}{\mathrm{d}t} = \frac{2\pi}{R_c\Omega_i}\left[\left(\frac{R_c\Omega_i}{2}\right)^2 r_0 + f\frac{E_c}{B}R_c\Omega_i - \frac{c_k^2}{r_0^3}\right] \\ v_{\phi 0} = \frac{r}{r_0} v_\phi + \frac{1}{2} R_c\Omega_i \left(\frac{r^2}{r_0} - r_0\right) \\ c_k = r^2\left(\frac{v_\phi}{r} + \frac{1}{2}R_c\Omega_i\right) \end{array}\right\} \tag{2.5}$$

where all parameters of position, speed, or time are dimensionless in units of R_c, v_T, or, $2\pi/\Omega_i$, respectively. Note that $\{r, v_r, v_\phi\}$ are input parameters, $\{r_0, v_{r0}, v_{\phi 0}\}$ are outputs, and $r_0 = r_0(r, v_r, v_\phi)$, $v_{r0} = v_{r0}(r, v_r, v_\phi)$, $v_{\phi 0} = v_{\phi 0}(r, v_r, v_\phi)$.

3 NUMERICAL CALCULATIONS FOR DISTRIBUTION FUNCTION AND BULK PROPERTIES

In the absence of collisions, Paper 1 tells us that the ion distribution function $f_i[\mathbf{r}(t), \mathbf{v}(t)]$ in phase space at any time t is determined by the initial distribution function $f_i(\mathbf{r}_0, \mathbf{v}_0)$ at $t = 0$:

$$f_i(\mathbf{r}, \mathbf{v}, t) = f_i(\mathbf{r}_0, \mathbf{v}_0, 0) = f_0 = \frac{n_0}{\pi} e^{-(v_{r0}^2 + v_{\phi 0}^2)} \tag{3.1}$$

Here, we still assume the initial ion distribution function to be Maxwellian. Using Eq.(2.2), we immediately find that

$$\left.\begin{array}{l} f_i(\mathbf{r}, \mathbf{v}, t) = \frac{n_0}{\pi} e^{-[v_r^2 + v_\phi^2 + (P_r - P_{r_0})]} = \\ = \frac{n_0}{\pi} e^{-\left[v_r^2 + v_\phi^2 - 2\frac{E_c}{B} R_c\Omega_i \int_r^{r_0} f(r)\mathrm{d}r\right]} \end{array}\right\} \tag{3.2}$$

in which P is dimensionless with $mv_T^2/2$, and $r_0 = r_0(r, v_r, v_\phi)$ is numerically calculated from Eq.(2.5). Using f_i, the following velocity moments can be expressed from the definitions:

$$\left.\begin{array}{l} n_i = \int f_i \mathrm{d}\mathbf{v} \\ \langle v_r\rangle = \frac{1}{n_i}\int v_r f_i \mathrm{d}\mathbf{v},\ \langle v_\phi\rangle = \frac{1}{n_i}\int v_\phi f_i \mathrm{d}\mathbf{v} \\ \langle v_r^2\rangle = \frac{1}{n_i}\int v_r^2 f_i \mathrm{d}\mathbf{v},\ \langle v_\phi^2\rangle = \frac{1}{n_i}\int v_\phi^2 f_i \mathrm{d}\mathbf{v} \\ \langle v_r^3\rangle = \frac{1}{n_i}\int v_r^3 f_i \mathrm{d}\mathbf{v},\ \langle v_\phi^3\rangle = \frac{1}{n_i}\int v_\phi^3 f_i \mathrm{d}\mathbf{v} \end{array}\right\} \tag{3.3}$$

The moments are obtained numerically by applying the Gauss-Hermite weight integrations. From there, the bulk parameters can be calculated as follows:

$$\left.\begin{array}{l} v_{\mathrm{d}r} = \langle v_r\rangle\ ,\ \ v_{\mathrm{d}\phi} = \langle v_\phi\rangle \\ T_r = 2\left(\langle v_r^2\rangle - \langle v_r\rangle^2\right) \\ T_\phi = 2\left(\langle v_\phi^2\rangle - \langle v_\phi\rangle^2\right) \\ p_{rr} = n_i T_r\ ,\ \ p_{\phi\phi} = n_i T_\phi \\ q_r = \langle v_r^3\rangle - \langle v_r\rangle^3 - \frac{3}{2}\langle v_r\rangle \cdot T_r\ , \\ q_\phi = \langle v_\phi^3\rangle - \langle v_\phi\rangle^3 - \frac{3}{2}\langle v_\phi\rangle \cdot T_\phi \end{array}\right\} \tag{3.4}$$

We made use of the numerical recipes in Fortran 77 [51] to develop a semi-numerical code used for the numerical simulations. The code contains subroutines to solve a set of differential-integral equations to produce simulation data of ion velocity distributions and transport parameters. The validity of the code was checked first of all against analytical solutions from Paper 1 under the $E \propto r$ case at $r = R_c$ and the time is

at $t/T = 3/4$ where $T = 2\pi/\omega$ and ω is the effective gyrofrequency defined in Paper 1. The error is within 9×10^{-6}. In addition, we also checked the fit of the bulk parameters between the analytical and numerical calculations. Except that in $t \in (0.2 \sim 0.3)$ and $t \in (0.7 \sim 0.8)$ the heat flow deviates from zero up to 0.0839, all the other properties have zero deviations.

We mention here that Fig. 1 should cover a reasonable range of ionospheric possibilities at least qualitatively. In addition to the simple Curve 1 case already discussed in Paper 1, Fig. 1 shows three typical types of radial electric field structures which are not proportional to the radial position:

(1) Curve 2: $E_r = -E_c(r/R_c)/[1 + 0.1\,(r/R_c)^3]$. Within $r = R_c$, E_r is proportional to r; outside $r = R_c$, E_r decreases to zero slowly relative to Curve 3.
(2) Curve 3: $E_r = -E_c(r/R_c)e^{-0.1(r/R_c)^3}$. Within $r = R_c$, E_r is proportional to r; outside $r = R_c$, E_r decreases to zero quickly relative to Curve 2.
(3) Curve 4: $E_r = -E_c e^{-(r/R_c-1)^2/0.1^2}$. At an arbitrary position in space ($r = R_c$ is taken as an example), there is an electric field jump.

We thus calculate the typical velocity distributions and associated transport properties under these different electric field variations in space. A flow chart describing the computer procedure used to solve the problem is given in Fig. 2.

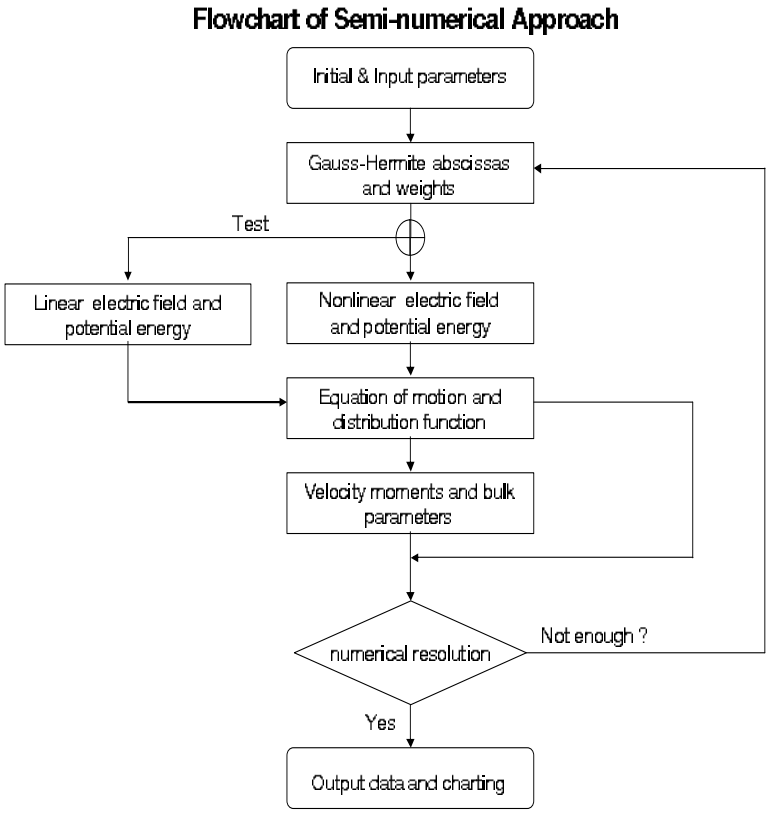

Fig. 2. Flowchart of the semi-numerical approach used for generalized nonlinear electric fields which are constant in time

4 ION DISTRIBUTION FUNCTIONS IN DIFFERENT CASES

Under three realistic, spatially inhomogeneous electric field structures (Curve 2-4) in Fig.1, we reply on the generalized semi-numerical "backward ray-tracking" code to calculate the ion velocity distributions and bulk parameters. The results are as follows.

4.1 Case 1: Slowly Disappearing E Versus r after Maximum

Fig.3 uses nine panels to show the evolution of the ion O^+ distribution function in velocity space from $t = 0$ to the same length of time in a magnetic gyro-period [$T = 2\pi/\Omega_i = 2\pi m/(eB)$]. Notice that this gyro-period is that of ions under zero electric field. So, it is not the actual "gyro-period" of ions gyrating under the electric field 2 in Fig. 1.

However, there may or may not be such a "gyro-period" shared by all particles in motion. In a field which does not change linearly along the radial direction, ions are not in phase. This is the difference from what Paper 1 describes: the motion of all ions are in phase under linear electric fields. This means in the present case that ions with different initial conditions move in different characteristics in space with their respective gyro-frequencies. Thus, when we use the phrase "guiding center (GC)" in the following text, we do not refer to the center of the distribution function for all ions as a whole, but only to the so called "center" of the dominant part of the distribution functions (maybe several parts) in velocity space.

Fig. 3 is plotted with two input parameters: the radial position is at $r = R_c$ and $E_c/B = 2$. Though the electric field is nonlinear in the radial direction, we notice that it contains a linear component: if r is small, the field turns out to be a linear electric field, meaning the charge density is still uniform close to the center of the space charge cylinder as discussed in Paper 1. Thus, we guess that the ion velocity distribution at $r = R_c$, a radial position not very far from and not very close to the center, should bring, more or less, the features of the distributions introduced in Paper 1. Let's have a close look at the figure.

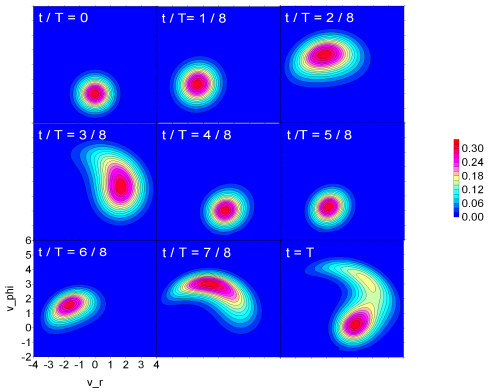

Fig. 3. Ion velocity distribution function versus time at $r = R_c$ and at $E_c/B = 2$ for $E_r = -E_c(r/R_c)/\left[1 + 0.1\,(r/R_c)^3\right]$. In all panels, $T = 2\pi/\Omega_i$

Firstly, the figure shows a similar rotation feature as that in Paper 1: the ion distribution function rotates continuously around some center related to the $\mathbf{E} \times \mathbf{B}$ drift on the v_ϕ-axis. The panels at $t/T = 3/8$ and $t = T$ illustrate that the center seems to be located at $v_\phi = 2$. We know from Chapter 2 that the $\mathbf{E} \times \mathbf{B}$ drift is $E_r/B = (E_c/B) \times (r/R_c) = 2$ at $r = R_c$. Secondly, all panels together show roughly a periodic change in sizes of the evolving ion distribution function. At first as in the panel at $t/T = 0$, the area of the distribution is small; then it increases, decreases, and increases, oscillating in time. This is exactly the feature shown in Paper 1 for the evolution of the ion distribution in time. Lastly, the gyration of ions appears to have the same effective gyro-frequency (ω) as that given in Paper 1: there, the value of ω turns out to be $\sim 1.9\Omega_i$ for $E_c/B = 2$. This means during one magnetic gyro-period ($1/\Omega_i$), ions have experienced approximately 2 rotations with the effective gyro-frequency ω. See the nine panels in Fig. 3: they roughly have rotated twice from $t = 0$ to $t = T = 2\pi/\Omega_i$.

Though with so many similar features to the case in Paper 1, Fig. 3 does tell us obvious differences of ion velocity distributions from that under the linear radial electric field structures. For example, because ions are no longer in

phase, the appearance of the distribution function does not keep the original "cake" shape at panel $t/T = 0$ they are evolving from, unlike that in Paper 1. At panel $t/T = 3/8$, the distribution function becomes teardrop-shaped; while at panel $t = T$, it is scattered to such a weird shape that a tail emerges out from the core body. Another related feature different from that in Paper 1 is: both the density and temperature are no longer keeping the same variations; more than that, each of them does not oscillate in the same way from one gyration to the other. For instance, it is impossible to find two panels in Fig. 3 which have areas (indicating ion density) or the diameters (indicating ion temperature), respectively, of the same size. Moreover, the so called "GC" speed never reaches twice the $\mathbf{E}\times\mathbf{B}$ drift as obtained in Paper 1. See panel $t/T = 2/8$. The "GC" speed is obviously lower than 4. Unlike the linear field case where ions at larger radius feel stronger electric force to accelerate them inward to higher speeds when deflected into the region of interest by the magnetic field, the nonlinear field we are using is localized and no ions outside several R_c are driven inward. Thus, ions with higher speeds are lacking in the region of interest. Naturally, the bulk speed of all ions is unable to touch the top of the circle delineated by the GC motion in velocity space around the $\mathbf{E}\times\mathbf{B}$ drift shown in Paper 1.

4.2 Case 2: Quickly Disappearing E Versus r after Maximum

If the space charge diffusion outside the region of interest is not as high as in Case 1, the ion velocity distribution function is still determined by the localized electric field structure in the region. Curve 3, on the one hand, is not much different from Curve 2 for small r and is still linear along the radial direction. This means the evolution of the distribution function should still have, more or less, the features given in Paper 1. On the other hand, at larger radius, the electric field falls to zero, just like in Curve 2. Thus, we can predict reasonably that the evolution of the distribution function should have, more or less, the features given in Case 1. See Fig. 4 for these similarities.

The nine panels show nearly the same evolving features as Case 1 in the gyration period, the top GC speed, the distribution shapes, etc. The only conspicuous difference lies in the tail shown in the last panel at $t = T$: the ion distribution appears to be larger even in the core and tail parts than that shown in Fig. 3. This may be explained by the fact that a narrower space charge boundary brings about a sharper drop in the electric field strength, which leads to fewer energetic ions in the tail to be deflected away by the $\mathbf{E}\times\mathbf{B}$ drift from the region of interest.

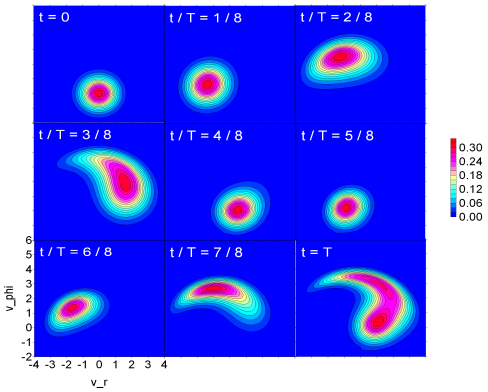

Fig. 4. Ion velocity distribution function versus time at $r = R_c$ and at $E_c/B = 2$ for $E_r = -E_c(r/R_c)e^{-0.1(r/R_c)^3}$. In all panels, $T = 2\pi/\Omega_i$

At this point, we would like to show another interesting feature the ion velocity distribution function reveals: a core-halo shaped appearance. This unexpected shape originates from the application of stronger electric field strengths, as shown in Fig. 5. With an increasing electric field, the ion distribution function first moves in velocity space as a whole. But at $E_c/B = 4$, the teardrop-shaped distribution is separated into two parts: a core continuing to move downward, and a halo peeling off but moving upward. The halo is flying away from the core distribution. In an enlarged figure given by Fig.4.4 below, the center of the halo is at $v_r = 1$ and $v_\phi = 7.3$ for $E_c/B = 6$. Different from the core-tail case, this core-halo distribution is directly related to the formation of an energetic ion beam.

If the electric field continues to increase, the halo flies away from its parental core as shown in panel $E_c/B = 5$. Noticeably, the core shrinks to a

smaller size than before giving off the halo. In an enlarged figure given by Fig. 9 below, numerical calculations show that the center of the halo is at $v_r = 1$ and $v_\phi = 7.3$.

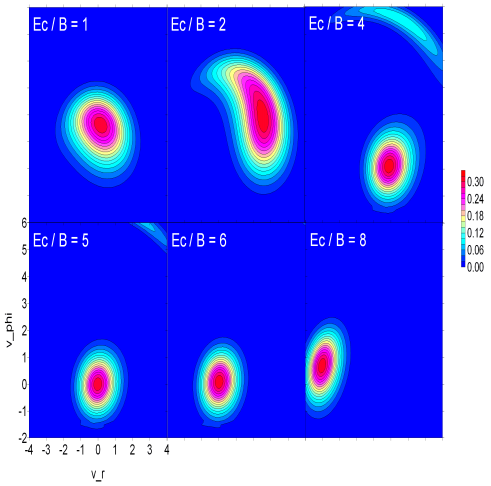

Fig. 5. Ion velocity distribution function versus E_c at $r = R_c$ and at $t = 3T/8$ (where $T = 2\pi/\Omega_i$) for $E_r = -E_c(r/R_c)e^{-0.1(r/R_c)^3}$.

4.3 Case 3: Sharp Changes in E Versus r

We intentionally choose $r = R_c$ as the layer (or surface) where space charges produce a δ-function-like radial electric field. Both inside and outside the layer, the electric field drops to zero abruptly (Curve 4 in Fig.1).

This kind of electric field structure brings about a few bizarre features to the ion velocity distribution function. First of all, at any time, the distributions are completely deformed in shape from the initial Maxwellian. However, generally speaking, the incomplete "bee"-shaped body is staying still at the initial position in velocity space, though some parts of the body move in time. An associated feature is that though there exists the strong electric field at $r = R_c$, no GC motion related to the $\mathbf{E} \times \mathbf{B}$ drift is seen to be triggered as happened in Cases 1 and 2. Both Figs. 6 and 7 confirms this static evolution of the distribution function in time, respectively. Finally, an ear-collar shaped distribution is evolving on the bee-shaped body. At panel $t/T = 1/8$ in Fig.6, a bigger LHS ear first develops. This ear extends wider in velocity space and then moves up to the top to meet with another smaller RHS ear which is also moving up from another side. At the same time, a collar is formed and moves downward while the ears move up. Fig. 7 depicts this process more clearly.

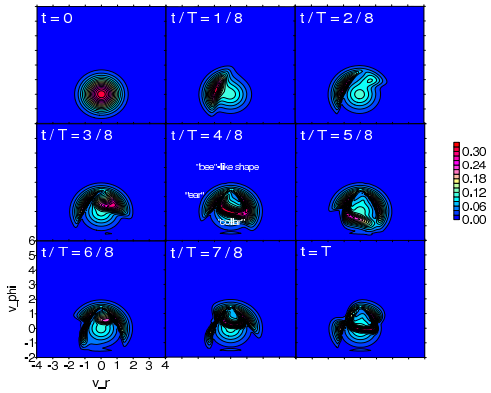

Fig. 6. Ion velocity distribution function versus time at $r = R_c$ and at $E_c/B = 2$ for $E_r = -E_c e^{-(r/R_c-1)^2/0.1^2}$: panels for time $t = 0 - T$. In all panels, $T = 2\pi/\Omega_i$. In the central panel, " 'bee-like' shape", "ear", "collar" are labeled.

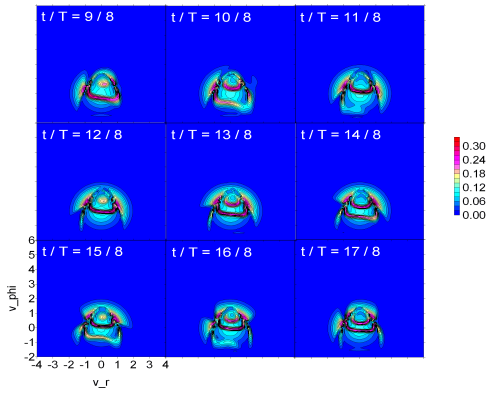

Fig. 7. Ion velocity distribution function versus time at $r = R_c$ and at $E_c/B = 2$ for $E_r = -E_c e^{-(r/R_c-1)^2/0.1^2}$: panels for time $t = T - 2T$. In all panels, $T = 2\pi/\Omega_i$.

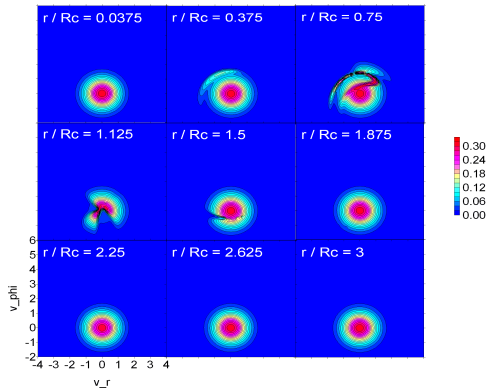

Fig. 8. Ion velocity distribution function versus radial position at $t = 7T/8$ (where $T = 2\pi/\Omega_i$) and at $E_c/B = 2$ for $E_r = -E_c e^{-(r/R_c-1)^2/0.1^2}$.

At this stage, it is intriguing to know the dependence of the ion velocity distribution function on the radial position. From the profile of the electric field structure, $E_r = -E_c \exp[-(r/R_c - 1)^2/0.1^2]$, we know that the field strength decreases to zero if r deviates far away from R_c. So, at both small or large r/R_c, there is no electric field locally to drive ions. Thus, either inside or outside the cylinder the ion distribution function should keep its initial Maxwellian form. Luckily, Fig. 8 reveals this feature: from panel $r/R_c = 0.0375$ to $r/R_c = 0.375$, we can see that the distribution functions are mainly Maxwellian at smaller radius. However, closer to $r/R_c = 1$, the ear-collar bee-shaped distribution is emerging from the Maxwellian till panel $r/R_c = 1.5$. After that, at larger radius the distribution returns to Maxwellian again.

4.4 Backmapping Phase-space Parameters

In case 2, a core-halo distribution function has been found under $E_c/B \geq 4$. The ions in the halo are more energetic with a much larger drift speeds. For example, at $E_c/B = 6$, $t/T = 3/8$, numerical calculations show that the center of the halo is at $v_r = 1$ and $v_\phi = 7.3$ in velocity space at the radial position $r = R_c$. This gives a perpendicular speed $v_\perp = \sqrt{v_r^2 + v_\phi^2} \sim \sqrt{54}$ which is 5.2 times the initial perpendicular speed. Accordingly, the perpendicular ion energy has increased to 27 times of the initial energy.

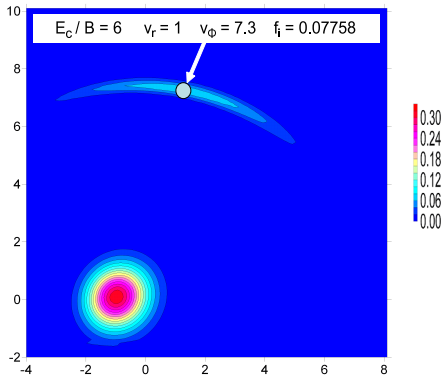

Fig. 9. Core-halo distribution function and its peak at $E_c/B = 6$ (in units of v_{th}) at $r = R_c$ and at $t = 3T/8$ (where $T = 2\pi/\Omega_i$) under the electric field structure $E_r = -E_c(r/R_c) \cdot e^{-0.1(r/R_c)^3}$.

The origin of these energetic ions has been found by using a back-tracing approach. By picking up a halo point in velocity space and then using the $\{v_r, v_\phi\}$ values as the initial conditions in the back-mapping equation of motion, we can immediately obtain $\{r_0, v_{r0}, v_{\phi 0}, \phi_0\}$ in phase space. Let's use the above velocity point $\{v_r = 1, v_\phi = 7.3\}$ in the halo as an example, at which the halo distribution function is maximal, $f_{i10} = 0.07758$ as shown in Fig. 9. The numerical results are shown in Fig. 10: this maximum halo distribution has contributions from all the ions with initial phase-space values designated by the curves from $t = 0$ to $t = 3T/8$, respectively.

4.5 Transport Properties

Various transport properties (density, average speeds, temperatures, heat flows, etc.) are numerically calculated from velocity moments of the ion velocity distributions. For a direct comparison, Fig.11 shows these bulk parameters under the first two nonlinear electric field structures.

The evolution of these parameters in time reveals a quasi-periodic feature under either electric

field structure. There is not much difference in the quasi-oscillations for the two different electric fields. However, the quasi-oscillations are not totally the same. For example, the electric field which drops more slowly outside the cylinder [electric field (1) in the figure] appears to give oscillations with higher amplitudes in density (n_i) and azimuthal components of the bulk properties (e.g., v_ϕ, T_ϕ, and q_ϕ). By contrast, the electric field which drops more quickly outside the cylinder [electric field (2) in the figure] triggers oscillations with higher amplitudes in the radial components of the bulk parameters (e.g., T_r and q_r). It deserves to be mentioned here that the existence of the heat flows indicates local temperature gradients in real space.

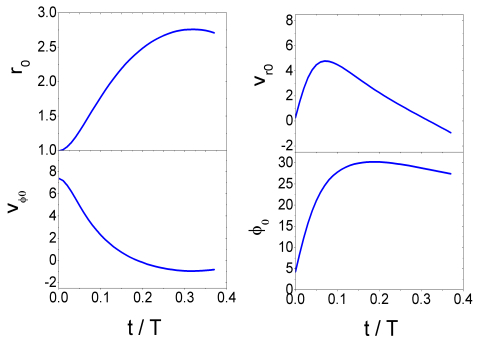

Fig. 10. Ion parameter spectra in phase space resulting in a halo distribution peak of $f_{i10} = 0.07758$ at $r = R_c$ and at $t = 3T/8$ (where $T = 2\pi/\Omega_i$) under the electric field structure used in Fig. 9 for $v_r = 1$ and $v_\phi = 7.3$.

Under the situation of the sharp electric field case, Fig. 12 shows two nine-panel plots. The upper nine panels tell us the evolution of the bulk parameters with time, while the lower nine ones show their changes as a function of radial position. A striking feature of the upper panels is that all bulk parameters oscillate relatively steadily with time in comparison to those under previous two electric fields. For example, they all have a time-average value plus a fluctuating component; and, the time-average values of both q_r and q_ϕ are around zero.

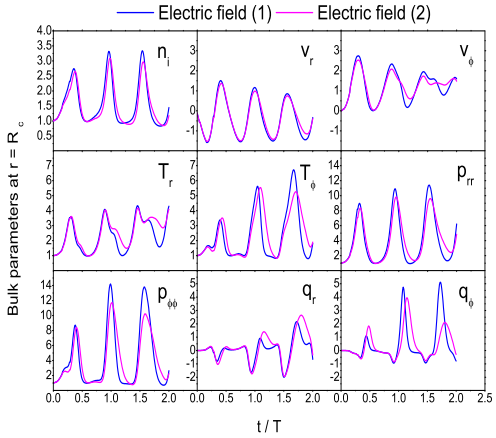

Fig. 11. Ion bulk properties as a function of time for two nonlinear electric field structures: (1) $E_r = -E_c(r/R_c)/[1 + 0.1(r/R_c)^3]$; (2) $E_r = -E_c(r/R_c)e^{-0.1(r/R_c)^3}$.

The lower nine panels describe that these bulk properties are localized ones. For example, outside $r = 2R_c$, they all turn out to be zero. However, in the region from $r = 0$ to $r = 2R_c$, the parameters changes violently. No doubt there are radial gradients for all of them.

5 SUMMARY AND DISCUSSION

Non-Maxwellian velocity distribution function and related observable transport parameters (e.g., bulk velocity, temperature, etc.) produced by different auroral electric field structures have been studied since the early seventies. Earlier studies had established that the ion velocity distributions under homogeneous electric fields can differ in important ways from the conventionally assumed Maxwellian (Gaussian) velocity distribution by becoming ring-shaped in velocity space under very strong electric field conditions [33]. In comparison to this homogeneous case, early studies had shown that the velocity distributions under an inhomogeneous electric field which increases linearly in a specific direction in space were found to be crescent-shaped (as opposed to

ring-shaped) in the velocity plane transverse to the magnetic field direction under similarly very strongly driven conditions [32,40].

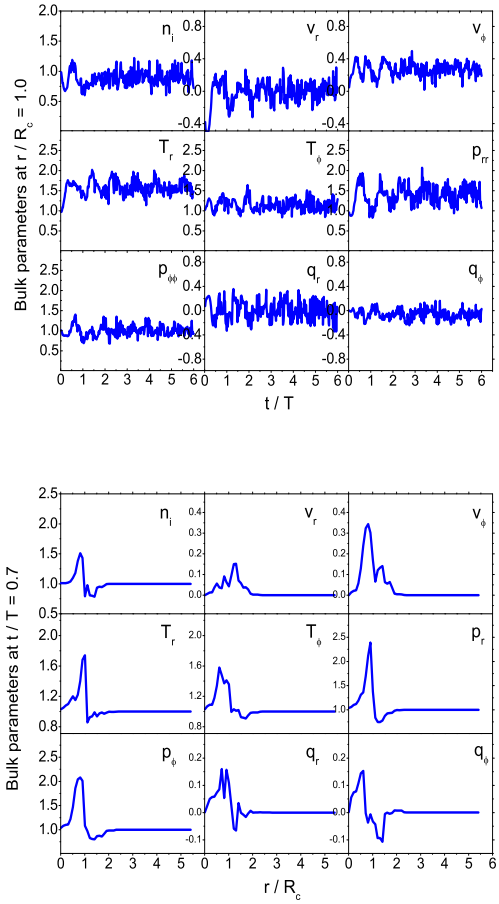

Fig. 12. Ion bulk properties under a nonlinear electric field structure $E_r = -E_c e^{-(r/R_c-1)^2/0.1^2}$. Upper 9 panels: as a function of time. Lower 9 panels: as a function of radial position.

However, the aurora often breaks down into elongated filaments that are aligned with the geomagnetic field. It is natural to infer from this that when important structures are found in the electrostatic fields they, too, will follow a cylindrical geometry. The present paper extends our previous work under a simple ionospheric electric field which increases linearly in the radial direction (Paper 1). We verified first of all the validity of the code by reproducing all the results given in Paper 1. After that, we calculated the ion velocity distributions and bulk properties under three realistic electric field models: (1) an electric field which is proportional to the radius inside a space charge cylinder but drops off slowly out side the cylinder; (2) an electric field which is still proportional to the radius inside a space charge cylinder but drops off more quickly out side the cylinder; and, (3) an electric field which is localized at the edge of the cylinder. In regimes where the electric field dropped outside a space-charge region, the evolving velocity distribution with time was found to have many possible types of shapes, such as, deformed pancake, horseshoe, teardrop, core-halo, etc. If the electric field dropped sharply on both sides of the boundary of a region, the distribution developed an ear-collar appearance with time. Under all electric field structures, the non-Maxwellian distributions and related transport parameters were localized to the region of an electric field. In this study, we also used a backmapping technique to find where those ions contributing to a specific distribution point in velocity space came from.

Though the present work offers both qualitative and quantitative insights into auroral ion distributions, as well as into their bulk properties as they are driven by different types of electric fields in auroral regions, much work is needed for more complicated situations and to explain important ionospheric phenomena measured by rockets and/or satellites. For one thing, the study should be extended to tackle an important issue in auroral physics: transverse ion energization and ion outflows in the formation of ion conics in velocity space. The first ion conic was measured by Satellite 1976-65B [52]. In that work, conic H^+ and O^+ ions were detected at about $1R_E$ in the northern dayside polar cusp. Since then, many satellites have observed ion conics in geospace (e.g., [53-56]. A widely accepted process for the evolution of ion conics is as follows [57-61]: at first, some kind of mechanism has to produce transverse ion heating; heated ions are then driven upward by the geomagnetic mirror force which is proportional to the transverse kinetic energy under the conservation of the first adiabatic invariant; the total velocity of the ions takes a conic appearance at higher altitudes;

the presence of parallel electric fields may contribute to a more complicated picture through "a pressure cooker" effect [59,62,63]. The mechanism underlying the transverse ion heating is not yet clear enough. Wave energization is one possibility, with a term to represent the perpendicular energy gain from the "wave-particle interactions (WPI)" in the conic equations [59]: $\mathrm{d}\mathcal{E}_\perp/\mathrm{d}t|_{\mathrm{WPI}}$. This term has been assumed constant (at 1 eV/s) for protons over the altitude range $0.1R_E < h < 1R_E$, and suggested to scale as $m^{\alpha-1}$ for heavy ions, where α is a power-law index from the spectral fit [64].

6 CONCLUSION

We solved ion velocities and transport properties under the collision-free condition in cylindrically symmetric, arbitrarily structured electric fields in auroral ionosphere. The work was developed from the previous work which dealt with a simple linear field in the radial direction in paper 1. We employed a backward mapping technique to numerically solve the Boltzmann-Vlasov equation under three arbitrarily chosen electric field configurations. The study presents following conclusions:

(1) In the presence of electric field, ion velocity distributions are no longer Maxwellian; that is, auroral ionosphere cannot retain an thermal equilibrium anymore;
(2) The electric field is able to trigger various shapes of non-Maxwellian distributions: in regimes where the electric field dropped outside the space-charge region, the evolving velocity distribution with time is found to have shapes like, deformed pancake, horseshoe, teardrop, core-halo; if the electric field drops sharply on both sides of the boundary of the region, the distribution develops into an ear-collar appearance with time;
(3) Once the electric field comes into being, the non-Maxwellian distributions and related transport parameters are localized only to the region where the electric field permeates.

In future, we hope to apply our model to the data-fit modelling for ongoing and future high-resolution observations.

ACKNOWLEDGEMENT

This work was funded by a research grant at the University of Saskatchewan in 2005-2008.

COMPETING INTERESTS

Authors have declared that no competing interests exist.

References

[1] Banaszkiewicz M, Ip W-H. The velocity distribution functions of oxygen and sulphur ions in the Io plasma torus. Adv. Space Res. 1993;13(10):331-335.

[2] Frank LA, Paterson WR. Return to Io by the Galileo spacecraft: Plasma observations. J. Geophys. Res. 2000;105(25):363-25,378.

[3] Cranmer SR. Solar wind acceleration in coronal holes. In: ESA SP-508. Proc. of the SOHO-11 symposium: From solar minimum to solar maximum. Davos, Switzerland. 2002;361-366.

[4] Steffl AJ. The Io plasma torus during the Cassini encounter with Jupiter: Temporal, radial and azimuthal variations. Ph.D. thesis. University of Colorado; 2005.

[5] Yermolaev I, Fedorov AO, Vaisberg OL, et al. Ion distribution dynamics near the Earth's bow shock: First measurements with the 2D ion energy spectrometer CORALL on the INTERBALL/Tail-probe satellite. Ann. Geophys. 1997;15(5):533-541.

[6] Meziane K, Wilber W, Hamza AM, et al. Upstream field-aligned beams: Results from Cluster. In: ESA SP-598. Proc. Cluster and Double Star sym. 5th Anniversary of Cluster in Space. Noordwijk, Netherlands. 2006;1-5.

[7] Yau AW, Whalen WB, Peterson WK, et al. Distribution of upflowing ionospheric ions in the high-altitude polar cap and

auroral ionosphere. J. Geophys. Res. 1984;89:5507-5522.

[8] St.-Maurice J-P, Hanson WB, Walker JCG. Retarding potential analyzer measurement of the effect of ion-neutral collisions on the ion velocity distribution in the auroral ionosphere. J. Geophys. Res. 1976;81(31):5438-5446.

[9] Lockwood M, Bromage BJI, Horne RB, et al. Non-Maxwellian ion velocity distributions observed using EISCAT. Geophys. Res. Lett. 1987;14:111-114.

[10] Burchill JK, Knudsen DJ, Bock BJJ, et al. Core ion interactions with BBELF, lower hybrid, and Alfvén waves in the high-latitude topside ionosphere. J. Geophys. Res. 2004;109:A01219.

[11] Knudsen DJ, Bock BJJ, Bounds SR, et al. Lower-hybrid cavity density depletions as a result of transverse ion acceleration localized on the gyroradius scale. J. Geophys. Res. 2004;109:A04212.

[12] Bock BJJ. Study of lower-hybrid cavities detected by the GEODESIC and OEDIPUS-C sounding rockets. M.Sc. Thesis, University of Calgary; 2005.

[13] Bernhardt PA, Erickson PJ, Lind FD, et al. Artificial disturbances of the ionosphere over the Millstone Hill incoherent scatter radar from dedicated burns of the space shuttle orbital maneuver subsystem engines. J. Geophys. Res. 2005;110:A05311.

[14] Ott E, Farley DT. Microinstabilities and the production of short-wavelength irregularities in the auroral F region. J. Geophys. Res. 1975;80:4599-4602.

[15] St-Maurice J-P. On a mechanism for the formation of VLF electrostatic emissions in the high latitude F region. Planet. Space Sci. 1978;26:801-816.

[16] St-Maurice J-P, Schunk RW. Ion velocity distributions in the high latitude ionosphere. Rev. Geophys. Space Phys. 1979;17:99-134.

[17] Raman RSV. Incoherent scattering of radar waves in the auroral ionosphere. Ph.D. thesis, University of Michigan; 1980.

[18] Raman RSV, St-Maurice J-P, Ong RSB. Incoherent scattering of radar waves in the auroral ionosphere. J. Geophys. Res. 1981;86:4751-4762.

[19] Akasofu S-I. Physics of magnetospheric substorms. Dordrecht, Holland; Boston: D. Reidel; 1977.

[20] Akasofu S-I. Energy coupling between the solar wind and the magnetosphere. Space Sci. Rev. 1981;28(2):121-190.

[21] Akasofu S-I. The aurora: an electrical discharge phenomenon surrounding the Earth. Rep. Prog. Phys. 1981;44(10):1123-1149.

[22] Kan JR, Akasofu S-I. Electrodynamics of solar wind-magnetosphere-ionosphere interactions. IEEE Trans. Plasma Sci. 1989;17(2):83-108.

[23] Lyon JG. The solar wind-magnetosphere-ionosph-ere system. Science 2000;288(16):1987-1991.

[24] Swift DW. The effect of electric fields and ion-neutral collisions on Thomson scatter spectra. J. Geophys. Res. 1975;80(1):4380-4382.

[25] Marklund G, Sandahl I, Opgenoorth H. A study of the dynamics of a discrete auroral arc. Planet. Space Sci. 1982;30(2):179-197.

[26] Moore TE, Chandler MO, Pollock CJ, et al. Plasma heating and flow in an auroral arc. J. Geophys. Res. 1996;101(A3):5279-5298.

[27] Earle GD, Kelley MC, Ganguli G. Large velocity shears and associated electrostatic waves and turbulence in the auroral F region. J. Geophys. Res. 1989;94(1):15,321-15,333.

[28] Alexeev II, Feldstein YI, Greenwald RA. Convection vortex at dayside of high latitude ionosphere. Phys. Chem. Earth 1997;22(7-8):691-696.

[29] Huang C-S, Sofko GJ, McWilliams KA, et al. SuperDARN observations of quasi-stationary mesoscale convection vortices in the dayside high-latitude ionosphere. J. Geophys. Res. 1998;103(A12):29,239-29,252.

[30] Pietrowski D, Lynch KA, Torbert RB, et al. Multipoint measurements of

large DC electric fields and shears in the auroral zone. Geophys. Res. Lett. 1999;26(22):3369-3372.

[31] Danielides MA, Kozlovsky A. Aurora vortex structures as a result of disturbed geomagnetic conditions. In: The Outer Heliosphere: The Next Frontiers. Eds.: K Scherer, H Fichtner, H Jörg Fahr, and E. Marsch. COSPAR Colloquiua Series, Amsterdam: Pergamon Press. 2001;11.

[32] St-Maurice J-P, Schunk RW. Behavior of ion velocity distributions for a simple collision model. Planet. Space Sci. 1974;21:1-18.

[33] Cole KD. Atmospheric excitation and ionization by ions in strong auroral and man-made electric fields. J. Atmo. Terr. Phys. 1971;33:1241-1249.

[34] Schunk RW, Walker JCG. Ion velocity distributions in the auroral ionosphere. Planet. Space Sci. 1972;20:2175-2191.

[35] Cole KD. Effects of crossed magnetic and spatially dependent electric fields on charged particles motion. Planet. Space Sci. 1976;24:515-518.

[36] Rothwell PL, Silevitch MB, Block LP, et al. Acceleration and stochastic heating of ions drifting through an auroral arc. J. Geophys. Res. 1992;97:19,333-19,339.

[37] Rothwell PL, Silevitch MB, Block LP, et al. Particle dynamics in a spatially varying electric field. J. Geophys. Res. 1995;100:14,875-14,886.

[38] Anastasiadis A, Daglis IA, Tsironis C. Ion heating in an auroral potential structure. Astron. Astrophys. 2004;419:793-799.

[39] Ganguli G, Lee YC, Palmadesso PJ. Kinetic theory for electrostatic waves due to transverse velocity shears. Phys. Fluids 1988;31(4):823-838.

[40] St-Maurice J-P, Winkler E, Hamza AM. Ionospheric ion velocity distributions and associated transport properties in the presence of auroral electric field gradients. J. Geophys. Res. 1994;99:19,527-19,548.

[41] Vogelsang H, Lühr H, Voelker H, et al. An ionospheric travelling convection vortex event observed by ground-based magnetometers and by VIKING. Geophys. Res. Lett. 1993;20:2343-2346.

[42] Baranoski GVG, Rokne JG, Shirley P, et al. Simulating the aurora. J. Visual. Comput. Animat. 2003;14:43-59.

[43] Schuck PW, Bonnell JW, Kintner PM. A review of lower hybrid solitary structures. IEEE Trans. Plasma Sci. 2003;31:1125-1177.

[44] Vandenplas PE, Gould RW. Equations of a hot inhomogeneous plasma model-I: Resonance frequencies of a cylindrical plasma column. Plasma Phys (J. Nucl. Energy Part C). 1964;6:449-458.

[45] Whealton JH, Woo S-B. Ion velocity distribution of a weakly ionized gas in a uniform electric field of arbitrary strength. Phys. Res. A. 1971;6(6):2319-2325.

[46] Roig FS, Schoutens JE. Remarks on the use of Boltzmann's equation for electrical conduction calculations in metal matrix and in situ composites. J. Mater. Sci. 1986;21:2767-2770.

[47] Date H, Shimozuma M. Boltzmann equation description of electron transport in an electric field with cylindrical or spherical symmetry. Phys. Rev. E. 2001;64:066410.

[48] Takahashi T, Morohashi K, Iwasawa N, et al. Kinetic simulation for infinitely long cylindrical high-beta plasma with field-null surface. J. Plasma Fusion Res. Series. 2004;6:485-488.

[49] Ma JZG, St.-Maurice J-P. Ion distribution functions in cylindrically symmetric electric fields in the auroral ionosphere: The collision-free case in a uniformly charged configuration. J. Geophys. Res. 2008;113:A05312 (Paper 1).

[50] Ma JZG, St.-Maurice J-P. Backward mapping solutions of the Boltzmann equation in cylindrically symmetric, uniformly charged auroral ionosphere. Astrophys. Space Sci. 2015;357:104.

[51] Press WH, Teukolsky SA, Vetterling WT, Flannery BP. Numerical Recipes in Fortran 77. 2nd Ed., Cambridge: Cambridge University Press; 1997.

[52] Sharp RD, Johnson RG, Shelley EG. Observations of an ionospheric acceleration mechanism procucing energetic (keV) ions

primarily normal to the geomagnetic field direction. J. Geophys. Res. 1977;82:3324-3328.

[53] Klumpar DM. A digest and comprehensive biblography on transverse auroral ion acceleration. In: Ion Acceleration in the Magnetosphere and Ionosphere. Eds.: T Chang, MK Hudson, JR Jasperse, RG Johnson, PM Kintner, M Schulz. Geophys. Mono. 1986;38:389-398.

[54] Ergun RE, Su Y-J, Andersson L, et al. Direct observation of localized parallel electric fields in a space plasma. Phys. Rev. Lett. 2001;87(4):045003.

[55] Ergun RE. Auroral particle acceleration by strong double layers. 45th Annual Meeting of the Division of Plasma Physics. Meeting ID: DPP03. Albuquerque, New Mexico; 2003.

[56] McFadden JP, Carlson CW, Ergun RE, et al. FAST observations of ion solitary waves. J. Geophys. Res. 2003;108(A4):8018.

[57] Mozer F. On the lowest-altitude S3-3 observations of electrostatic shocks and parallel electric fields. Geophys. Res. Lett. 1980;7:1097-1098.

[58] Mozer F, Cattell C, Lysak R, et al. Satellite measurements and theories of low altitude auroral particle acceleration. Space Sci. Rev. 1980;27:155-213.

[59] Gorney DJ, Chiu YT, Croley DR. Trapping of ion conics by downward parallel electric fields. J. Geophys. Res. 1985;90(A5):4205-4210.

[60] Lysak RL. Ion acceleration by wave-particle interaction. In: Ion acceleration in the magnetosphere and ionosphere. AGU Geophys. Mono. 1986;38:261-270.

[61] Wu X-Y, Horwitz JL, Tu J-N. Dynamic fluid kinetic (DyFK) simulation of auroral ion transport: Synergistic effects of parallel potentials, transverse ion heating, and soft electron precipitation. J. Geophys. Res. 2002;107(A10):1283.

[62] Barakat AR, Barghouthi IA. The effect of wave-particle interactions on the polar wind O^+. Geophys. Res. Lett. 1994;21(21):2279-2282.

[63] Wu X-Y. Auroral ionospheric ion upflows and outflows: Satellite observations and dynamic fluid-kinetic simulations. Ph.D. thesis, University of Alabama (Hunts-ville); 2000.

[64] Lund EJ, Möbius E, Ergun RE, et al. Mass-dependent effects in ion conic production: The role of parallel electric fields. Geophys. Res. Lett. 1999;26(24):3593-3596.

Peer-review history:
The peer review history for this paper can be accessed here:
http://sciencedomain.org/review-history/16539